




Driving-induced resonance narrowing in a strongly coupled cavity-qubit systemEyal Buks ¹, Paul Brookes ², Eran Ginossar,³ Chunqing Deng,^{4,*} Jean-Luc F. X. Orgiazzi,⁴
Martin Otto ⁴ and Adrian Lupascu⁴¹*Andrew and Erna Viterbi Department of Electrical Engineering, Technion, Haifa 32000, Israel*²*Department of Physics and Astronomy, University College London, Gower Street, London, WC1E 6BT, United Kingdom*³*Advanced Technology Institute and Department of Physics, University of Surrey, Guildford, GU2 7XH, United Kingdom*⁴*Institute for Quantum Computing, University of Waterloo, Waterloo, Ontario, Canada N2L 3G1*

(Received 26 February 2020; revised 1 August 2020; accepted 14 September 2020; published 26 October 2020)

We study a system consisting of a superconducting flux qubit strongly coupled to a microwave cavity. Externally applied qubit driving is employed in order to manipulate the spectrum of dressed states. We observe resonance narrowing in the region where the splitting between the two dressed fundamental resonances is tuned to zero. The narrowing in this region of overlapping resonances can be exploited for long-time storage of quantum states. In addition, we measure the response to strong cavity mode driving, and find a qualitative deviation between the experimental results and the predictions of a semiclassical model. On the other hand, good agreement is obtained using theoretical predictions obtained by numerically integrating the master equation governing the system's dynamics. The observed response demonstrates a process of a coherent cancellation of two metastable dressed states.

DOI: [10.1103/PhysRevA.102.043716](https://doi.org/10.1103/PhysRevA.102.043716)**I. INTRODUCTION**

The spectral response of a variety of both classical and quantum systems near an isolated resonance is often well described by the Breit-Wigner model [1]. In this description the lifetime of an isolated resonance can be determined from its linewidth. A variety of intriguing effects may occur in regions where resonances overlap [2]. For example, both linewidth narrowing and broadening have been observed with systems having overlapping resonances [3]. These effects are attributed to interference between different processes contributing to damping [4,5]. Destructive interference gives rise to linewidth narrowing, whereas the opposite effect of broadening occurs due to constructive interference.

These effects have been demonstrated in a wide variety of both classical and quantum systems. In the classical domain narrowing has been observed with resonators having two overlapping resonances for which the frequency separation is smaller than the resonances' bandwidth [7–9]. Closely related processes occur in the quantum domain with systems having overlapping resonances. In some cases this overlap is obtained by static tuning of the system under study. One well-known example is the Purcell effect [10], which is observed when atoms interact with light confined inside a cavity. In such cavity quantum electrodynamics (CQED) systems, both linewidth narrowing and broadening occur when the atomic and cavity mode resonances overlap. Other examples of static tuning giving rise to linewidth narrowing and broadening due to overlapping resonances have been reported in [11,12].

Closely related processes occur in atomic systems exhibiting electromagnetically induced transparency (EIT) [13,14]. However, tuning into the region of EIT is commonly based on external driving (rather than static tuning), which can be used for manipulating the spectrum of the dressed states. Both linewidth narrowing and broadening have been observed in such systems in the region where the dressed spectrum contains overlapping resonances. Commonly, a broadened resonance is referred to as a bright state, whereas the term dark state refers to a narrowed resonance. The slow propagation speed associated with dark states [15] can be exploited for long term storage of quantum information [16].

Here we report on a linewidth narrowing that is experimentally observed in a superconducting circuit composed of a microwave resonator and a Josephson flux qubit [17,18]. The qubit under study, which is strongly coupled [19–22] to a coplanar waveguide (CPW) microwave resonator [6,20,23–27], is shown in Figs. 1(a) and 1(b). The strong coupling gives rise to a dispersive splitting of the cavity mode resonance. We find that this frequency splitting can be controlled by applying a monochromatic driving to the flux qubit [see Fig. 1(b)]. The effect of linewidth narrowing, which is discussed below in Sec. IV, is observed when the frequency and power of qubit driving are tuned into the region where the frequency splitting vanishes. In this region the measured linewidth becomes significantly smaller than the linewidth of the decoupled cavity resonance by a factor of up to 20.

While the linewidth narrowing effect is induced by qubit driving, a variety of other nonlinear effects can be observed with strong cavity mode driving [28–45]. In Sec. V we focus on the line shape of the cavity transmission in the nonlinear region. The experimental results are compared with predictions of a semiclassical theory. We find that good agreement

*Present address: Alibaba Quantum Laboratory, Alibaba Group, Hangzhou, Zhejiang 311121, People's Republic of China.

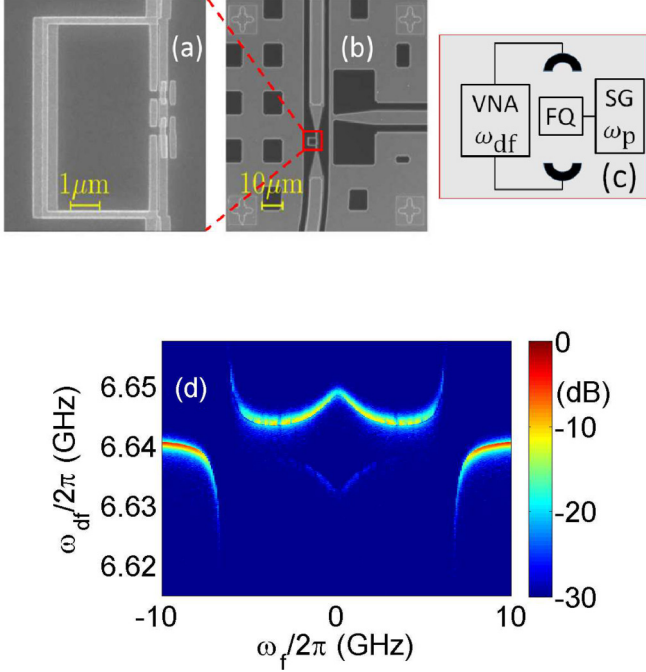


FIG. 1. The device. (a) Electron micrograph of the flux qubit. (b) Zoom out electron micrograph showing the qubit embedded in the CPW resonator and its local flux control line. (c) Sketch of the experimental setup. The cavity transmission is measured using a vector network analyzer (VNA). Monochromatic flux qubit (FQ) driving is applied using a signal generator (SG). (d) The measured cavity transmission (in dB units) vs $\omega_f/2\pi$ (magnetic field detuning from the symmetry point) and $\omega_{df}/2\pi$ (cavity driving frequency). The power injected into the cavity is -112 dBm. For the device under study $\omega_c/2\pi = 6.6408$ GHz, $\omega_\Delta/2\pi = 1.12$ GHz, $g/2\pi = 0.274$ GHz, and $\gamma_c/\omega_c = 1.1 \times 10^{-5}$. The relaxation time $T_1 = 1.2 \mu\text{s} (1 + 0.45 \text{ ns} \times |\omega_f|)$ is obtained from energy relaxation measurements, and the rate $T_2^{-1} = 4.5 \text{ MHz} (1 + 44 |\omega_f|/\omega_a)$ is obtained from Ramsey rate measurements [6]. The empirical expressions for both T_1 and T_2 are obtained using approximate interpolation.

can be obtained only in the limit of relatively small driving amplitudes. For higher driving amplitudes, better agreement is obtained with theoretical predictions derived by numerical integration of the master equation for the coupled system.

II. EXPERIMENTAL SETUP

The investigated device [6] [see Figs. 1(a) and 1(b)] contains a CPW cavity resonator weakly coupled to two ports that are used for performing microwave transmission measurements [see Fig. 1(c)]. A persistent current flux qubit [17], consisting of a superconducting loop interrupted by four Josephson junctions, is inductively coupled to the fundamental half-wavelength mode of the CPW resonator. We used a CPW line terminated by a low inductance shunt for qubit driving [see Figs. 1(b) and 1(c)]. We fabricated the device on a high resistivity silicon substrate in a two-step process. In the first step, the resonator and the control lines are defined using optical lithography, evaporation of a 190 nm thick aluminum layer, and liftoff. In the second step, a bilayer resist is patterned by electron-beam lithography. Subsequently,

shadow evaporation of two aluminum layers, 40 and 65 nm thick, respectively, followed by liftoff define the qubit junctions. The chip is enclosed inside a copper package, which is cooled by a dilution refrigerator to a temperature of $T = 23$ mK. We employed both passive and active shielding methods to suppress magnetic field noise. While passive shielding is performed using a three-layer high permeability metal, an active magnetic field compensation system placed outside the cryostat is used to actively reduce low-frequency magnetic field noise. We used a set of superconducting coils to apply dc magnetic flux. Qubit state control, which is employed in order to measure the qubit longitudinal T_1 and transverse T_2 relaxation times, is performed using shaped microwave pulses. Attenuators and filters are installed at different cooling stages along the transmission lines for qubit control and readout. A detailed description of sample fabrication and experimental setup can be found in [6,24].

III. THE DISPERSIVE REGION

The circulating current states of the qubit are labeled as $|\curvearrowright\rangle$ and $|\curvearrowleft\rangle$. The coupling between the cavity mode and the qubit is described by the term $-g(A + A^\dagger)(|\curvearrowright\rangle\langle\curvearrowleft| - |\curvearrowleft\rangle\langle\curvearrowright|)$ in the system Hamiltonian, where A (A^\dagger) is a cavity mode annihilation (creation) operator, and g is the coupling coefficient. In the presence of an externally applied magnetic flux, the energy gap $\hbar\omega_a$ between the qubit ground state $|-\rangle$ and first excited state $|+\rangle$ is approximately given by $\hbar\omega_a = \hbar\sqrt{\omega_f^2 + \omega_\Delta^2}$, where $\omega_f = (2I_{cc}\Phi_0/\hbar)(\Phi_e/\Phi_0 - 1/2)$, I_{cc} ($-I_{cc}$) is the circulating current associated with the state $|\curvearrowright\rangle$ ($|\curvearrowleft\rangle$), $\Phi_0 = h/2e$ is the flux quantum, Φ_e is the externally applied magnetic flux, and $\hbar\omega_\Delta$ is the qubit energy gap for the case where $\Phi_e/\Phi_0 = 1/2$.

In the dispersive region, i.e., when $g/|\Delta| \ll 1$ where $\Delta = \omega_c - \omega_a$ and ω_c is the cavity mode angular frequency, the coupling between the cavity mode and the qubit gives rise to a resonance splitting. The steady state cavity mode response for the case where the qubit occupies the ground (first excited) states is found to be equivalent to the response of a mode having effective complex cavity angular resonance frequency Υ_- (Υ_+), where $\Upsilon_\pm = \Upsilon_c \pm \Upsilon_{BS} \pm \Upsilon_{ba}$, $\Upsilon_c = \omega_c - i\gamma_c$ is the cavity mode intrinsic complex angular resonance frequency, with ω_c being the angular resonance frequency, γ_c is the linear damping rate, and $\omega_{BS} = g_1^2/(\omega_c + \omega_a)$ is the Bloch-Siegert shift [21]. The term Υ_{ba} is given by [34,45–47]

$$\Upsilon_{ba} = -\frac{g_1^2}{\Delta} \frac{1 - \frac{i}{\Delta T_2}}{1 + \frac{1}{\Delta^2 T_2^2} + \frac{4g_1^2 T_1 E_c}{\Delta^2 T_2}}, \quad (1)$$

where $g_1 = g/\sqrt{1 + (\omega_f/\omega_\Delta)^2}$ is the flux dependent effective coupling coefficient, $T_1 = \gamma_1^{-1}$ and $T_2 = \gamma_2^{-1}$ are the qubit longitudinal and transverse relaxation times, respectively, and E_c is the averaged number of photons occupying the cavity mode. Note that the imaginary part of Υ_\pm represents the effect of damping and the term proportional to E_c gives rise to nonlinearity. In the dispersive approximation this term is assumed to be small, i.e., $E_c \ll \Delta^2 T_2 / 4g_1^2 T_1$. Note also that when $\Delta T_2 \gg 1$ the term Υ_{ba} gives rise to a shift in the mode angular frequency approximately given by $\mp\chi$, where

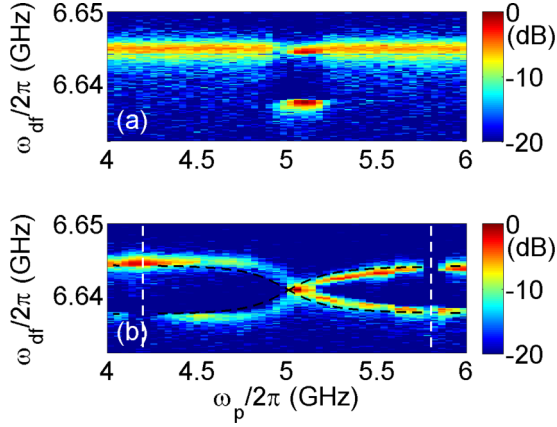


FIG. 2. The effect of qubit driving. Cavity transmission in dB units as a function of qubit driving frequency $\omega_p/2\pi$ and cavity driving frequency $\omega_{df}/2\pi$. The qubit driving amplitude Ω_q in (b) is 100 times larger compared with the values used in (a). For both plots the qubit frequency is given by $\omega_a/2\pi = 5$ GHz. The overlaid black dotted line in (b) is obtained by numerically calculating the transition frequencies between the lowest-lying eigenvalues of the Hamiltonian (A1) using the following parameters: $\Omega_q/2\pi = 0.5$ GHz, $\omega_c/2\pi = 6.6408$ GHz, $\omega_\Delta/2\pi = 1.12$ GHz, $\omega_f/2\pi = 4.9$ GHz, $\omega_a/2\pi = 5.0$ GHz, and $g_1/2\pi = 0.150$ GHz.

$\chi = g_1^2/\Delta$, and to a Kerr coefficient approximately given by $\pm(g_1^4/\Delta^3)(4T_1/T_2)$.

Network analyzer measurements of the cavity transmission are shown in Fig. 1(d). In the region where $\Delta > 0$ (i.e., the middle section of the panel where $|\omega_f| < \sqrt{\omega_c^2 - \omega_\Delta^2}$) two peaks are seen in the cavity transmission, the upper one corresponds to the case where the qubit mainly occupies the ground state, whereas the lower one, which is weaker, corresponds to the case where the qubit mainly occupies the first excited state.

IV. QUBIT DRIVING

The flux qubit is driven by injecting a signal having angular frequency ω_p and amplitude Ω_q into the transmission line inductively coupled to the qubit [see Figs. 1(b) and 1(c)]. Network analyzer measurements of the cavity transmission as a function of ω_p for two fixed values of qubit driving amplitude Ω_q are shown in Figs. 2(a) and 2(b). For both plots the qubit transition frequency is flux tuned to the value $\omega_a/2\pi = 5$ GHz. The frequency separation between the two resonances that are shown in Fig. 2 is consistent with what is expected from the above-discussed dispersive shift $\mp\chi$, where $\chi = g_1^2/\Delta$. As can be seen from Fig. 2, the visibility of the resonance corresponding to the qubit occupying the excited state at 6.637 GHz is affected by both angular frequency ω_p and amplitude Ω_q of qubit driving. These dependencies are attributed to driving-induced qubit depolarization.

The comparison between Fig. 2(a) and 2(b), for which the qubit driving amplitude Ω_q is 100 times higher, reveals some nonlinear effects. One example is a nonlinear process of frequency mixing of the externally applied driving tones, which gives rise to pronounced features in the measured cavity transmission when ω_p is tuned close to the values

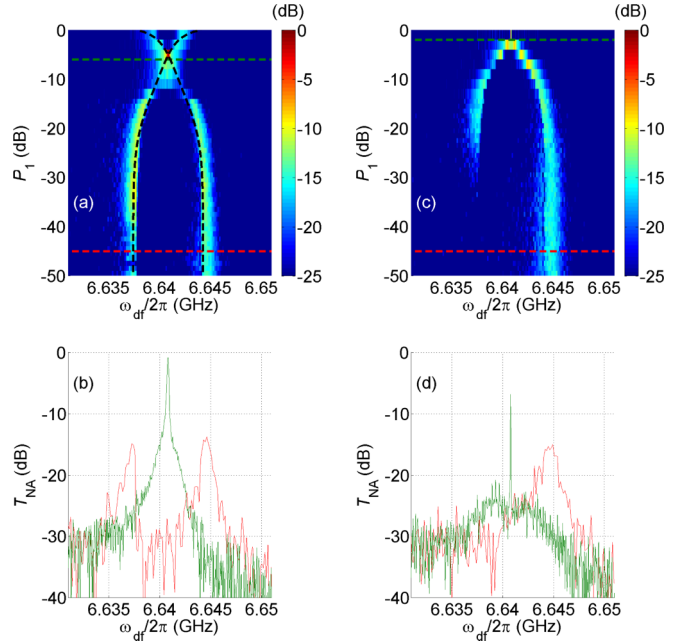


FIG. 3. Dependence on qubit driving amplitude. The driving frequency is $\omega_p/2\pi = 5.16$ GHz in (a) and (b) and $\omega_p/2\pi = 5.52$ GHz in (c) and (d). Cavity transmission in dB units as a function of cavity driving frequency $\omega_{df}/2\pi$ and amplitude (in logarithmic scale) $P_1 = 20 \log_{10}(\Omega_q/\Omega_{q,0})$ are shown in (a) and (c). Cross sections taken at values of P_1 indicated by colored horizontal dotted lines in (a) and (c) are shown using the corresponding colors in (b) and (d). The overlaid black dotted line in (a) is obtained by numerically calculating the transition frequencies between the eigenvalues of the Hamiltonian (A1) using the following parameters: $\omega_p/2\pi = 5.16$ GHz, $\Omega_{q,0}/2\pi = 2.4$ GHz, $\omega_\Delta/2\pi = 1.12$ GHz, $\omega_f/2\pi = 4.873$ GHz, $\omega_a/2\pi = 5.000$ GHz, and $g_1/2\pi = 0.150$ GHz.

$(\omega_a + \omega_c)/2 = 2\pi \times 5.8$ GHz and $(3\omega_a - \omega_c)/2 = 2\pi \times 4.2$ GHz [see the overlaid vertical white dotted lines in Fig. 2(b)].

The dependence of cavity transmission on qubit driving amplitude Ω_q with a fixed driving frequency of $\omega_p/2\pi = 5.16$ GHz ($\omega_p/2\pi = 5.52$ GHz) is depicted in Figs. 3(a) and 3(b) [Figs. 3(c) and 3(d)]. Cross sections of the color-coded plots shown in Figs. 3(a) and 3(c) (corresponding to different values of the qubit driving amplitude Ω_q) are displayed in Figs. 3(b) and 3(d).

As can be seen from the cross sections shown in Figs. 3(b) and 3(d), the cavity mode resonance line shapes exhibit hardening and softening effects (corresponding to positive and negative Kerr coefficient, respectively) in some region of the qubit driving amplitude Ω_q . Similar behavior is presented in Fig. 3 of Ref. [46], which exhibits cavity mode resonance line shapes of the same device in the absence of qubit driving. However, while the nonlinearity observed in Ref. [46] is induced by cavity driving, the one shown in Fig. 3(b) is induced by qubit driving.

The cavity driving-induced nonlinearity reported in Ref. [46] is well described by the above-discussed Kerr coefficients that can be calculated using Eq. (1) (see also Eqs. (4) and (A94) of Ref. [46]). As is argued below, similar nonlinearity can be obtained due to qubit driving. In the rotating wave approximation (RWA) the Hamiltonian \mathcal{H}_0 of the closed

system (consisting of a driven qubit and a coupled cavity mode) in a frame rotated at the qubit driving angular frequency ω_p is found to be given by [see Eqs. (A7)–(A9) of Appendix A] [48–54]

$$\hbar^{-1}\mathcal{H}_0 = (\omega_R/2)\Sigma'_z - \Delta_{pc}A^\dagger A + (g'/2)(A\Sigma'_- + \Sigma'_+A^\dagger), \quad (2)$$

where $\omega_R = \sqrt{\Omega_q^2 + 4\Delta_{pa}^2}$ is the Rabi frequency, $\Delta_{pa} = \omega_p - \omega_a$, and $\Delta_{pc} = \omega_p - \omega_c$. The operators Σ'_\pm and Σ'_z , which are defined by Eq. (A5), represent qubit operators in the basis of dressed states. This Hamiltonian (2) has the same structure as the Hamiltonian in the RWA of the same system in the absence of qubit driving (see Eq. (A13) of Ref. [46]). However, while for the case of no qubit driving the crossing point occurs when the qubit angular frequency ω_a coincides with the cavity mode angular frequency ω_c , the condition $\Delta_{pc} = \pm\omega_R$ is satisfied at the crossing point of the driven system.

The transformed Hamiltonian [34] $\mathcal{H}_T = U\mathcal{H}_0U^\dagger$ [see Eq. (2)], where the unitary operator U is given by $U = \exp[(\mathcal{N}^{-1/2}\mathcal{S}/2)\tan^{-1}(g'\mathcal{N}^{1/2}/\Delta_R)]$ and where $\Delta_R = \omega_R + \Delta_{pc}$, $\mathcal{N} = A^\dagger A + (1 + \Sigma'_z)/2$, and $\mathcal{S} = A\Sigma'_- - A^\dagger\Sigma'_+$ is given by (constant terms are disregarded)

$$\begin{aligned} \hbar^{-1}\mathcal{H}_T = & \left(-\Delta_{pc} + \xi\Sigma'_z - \frac{g'^4(1 + A^\dagger A\Sigma'_z)}{12\Delta_R^3} \right) A^\dagger A \\ & + \frac{(\omega_R + \xi)\Sigma'_z}{2} + O\left[\left(\frac{g'}{\Delta_R}\right)^5\right], \end{aligned} \quad (3)$$

where $\xi = [g'^2/(4\Delta_R)][1 - g'^2/(3\Delta_R^2)]$. Both hardening and softening effects are attributed to the term proportional to $A^\dagger AA^\dagger A\Sigma'_z$ in Eq. (3).

The term proportional to $A^\dagger A$ in the Hamiltonian (3) can be used to determine the shift in resonances that is induced by qubit driving. However, the calculated shift does not exhibit a good agreement with the measured shift shown in Figs. 2 and 3. The inaccuracy is attributed to throwing away counter-rotating terms of the form $A\Sigma'_+$ and $A^\dagger\Sigma'_-$ in the derivation of the Hamiltonian (2). Much better agreement is obtained by numerically calculating the eigenvalues of the Hamiltonian (A1). The results of this calculation are displayed in Figs. 2(b) and 3(a) by the overlaid black dotted lines. The parameters that have been assumed for the calculation are listed in the captions of Figs. 2 and 3.

As can be seen from both Fig. 2(b) and the green-colored cross sections shown in Figs. 3(b) and 3(d), in some regions of qubit driving parameters the two dressed fundamental resonances overlap. In the overlap region, a pronounced linewidth narrowing is observed [see Figs. 3(b) and 3(d)].

In Appendix A we show that the observed changes in linewidth of resonances can be qualitatively attributed to the Purcell effect for dressed states. In particular, both narrowing and broadening are demonstrated by Eqs. (A14) and (A15) below. However, the analytical expressions given by Eqs. (A14) and (A15), which have been obtained by assuming the limit of weak coupling and by employing the RWA, are not applicable in the region where the linewidth narrowing is experimentally observed. Consequently, direct comparison between theoretical predictions based on Eqs. (A14) and (A15) and data yields poor agreement. Moreover, the relatively intense driving in the region where the linewidth narrowing is experimentally

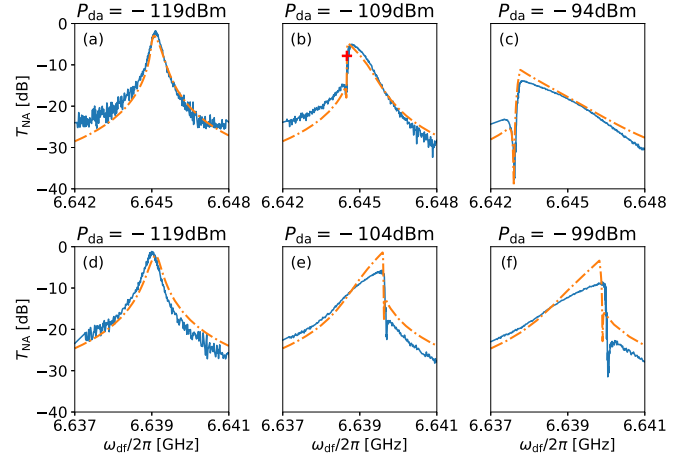


FIG. 4. Nonlinear response to cavity driving. The cavity transmission T_{NA} is measured as a function of cavity driving frequency $\omega_{df}/2\pi$ for different values of the cavity driving power P_{da} . These data are compared with a numerical calculation of the steady state of the Lindblad master equation (dashed red line), which is detailed in Appendix C. In (a)–(c) the frequency $\omega_f/2\pi$ is flux tuned to 5.5 GHz, and in (d)–(f) to 7.8 GHz. Different values of γ_c are used at each drive power to account for the increase in the quality factor of the cavity with occupation. We use $\gamma_c =$ (a) 0.314, (b) 0.251, (c) 0.126, (d) 0.314, (e) 0.251, and (f) 0.126 MHz.

observed gives rise to stochastic transitions between qubit states [55]. These stochastic transitions, which may give rise to the effect of motional narrowing [56–60], cannot be adequately accounted for using the semiclassical approximation. Note that these phenomena are closely related to the effect of driving-induced spin decoupling (e.g., Fig. 7.27 of Ref. [61]).

Numerical analysis based on the stochastic Schrödinger equation is described below in Appendix B. We find that the effect of narrowing can be numerically reproduced provided that both qubit and cavity driving amplitudes are sufficiently large. The analysis in this region is challenging, since relatively long integration times are needed to achieve convergence. As can be seen from Figs. 6 and 7, in the region where narrowing is numerically reproduced, the system becomes multistable.

V. CAVITY DRIVING

The nonlinear response of a microwave cavity coupled to a transmon superconducting qubit has recently been studied in Ref. [62]. The experimental results, together with theoretical analysis [45,63], indicate that the response to strong cavity driving is affected by the significant coherent driving of the qubit as well as by the stochastic transitions between qubit states. The effect of cavity driving can be characterized by a dephasing rate and by a measurement rate. Both rates have been numerically calculated and analytically estimated in Ref. [55].

Measurements of the cavity transmission T_{NA} of our device as a function of cavity driving frequency $\omega_{df}/2\pi$ and power P_{da} are shown in Fig. 4. No qubit driving is applied during these measurements. We demonstrate nonlinearity of the softening type in Figs. 4(a)–4(c), whereas hardening is

demonstrated in Figs. 4(d)–4(f). We obtained the data shown in Fig. 4 by sweeping the cavity driving frequency $\omega_{\text{dr}}/2\pi$ upwards. Almost no hysteresis is observed when the sweeping direction is flipped.

The measured cavity transmission T_{NA} can be compared with theoretical predictions based on the semiclassical approximation. Such a comparison has been performed in Ref. [46] based on data that has been obtained from the same device. Good quantitative agreement was found in the region of relatively small cavity driving amplitudes [46].

However, when the cavity is strongly driven, the nonlinearity introduced to the system by the qubit causes the onset of bistability and the semiclassical approximation alone is unable to reproduce the cavity transmission. This is because, despite accurately modeling the fixed points, which henceforth are referred to as the bright and dim metastable states (see Fig. 5), the semiclassical equations of motion give no information regarding the occupation probabilities of the two metastable states in the overall state of the system, which can be written as

$$\rho = p_b \rho_b + p_d \rho_d, \quad (4)$$

where ρ_b (ρ_d) and p_b (p_d) represent the bright (dim) state and its probability respectively.

The experimental results shown in Fig. 4 exhibit a sharp dip in cavity transmission T_{NA} at drive powers above -109 dBm. A very similar feature has been experimentally observed before in [62] and theoretically discussed in Refs. [45,63], for which the full quantum theory of the single nonlinear oscillator has been developed in [64]. The origin of this dip is the destructive interference between the two metastable states. Since the system is coupled to an external reservoir, fluctuations in the quantum state ensue and occasionally cause major switching events between the bright and dim states. When the complex amplitude of the cavity state is averaged over an ensemble of many such switching events, there is typically a narrow region in the frequency-power space where the two complex amplitudes partially cancel each other. By using the Lindblad master equation to model the system, we are able to take account of these fluctuations which cause these switching events and we produce the numerical fits seen in Fig. 4. Comparison between the predictions derived from the numerical integration of the master equation and the ones analytically derived from the semiclassical equations of motion is shown in Fig. 5.

VI. SUMMARY

Our main finding is the linewidth narrowing that is obtained by applying intense qubit driving. The effect is experimentally robust, however, its theoretical modeling is quite challenging. Further study is needed to explore the possibility of exploiting this effect for long-time storage of quantum information. We also find that bistability, which is predicted by the semiclassical model for monochromatic cavity driving, is experimentally inaccessible. This effect and related observations can be satisfactorily explained using numerical integration of the master equation for the coupled system.

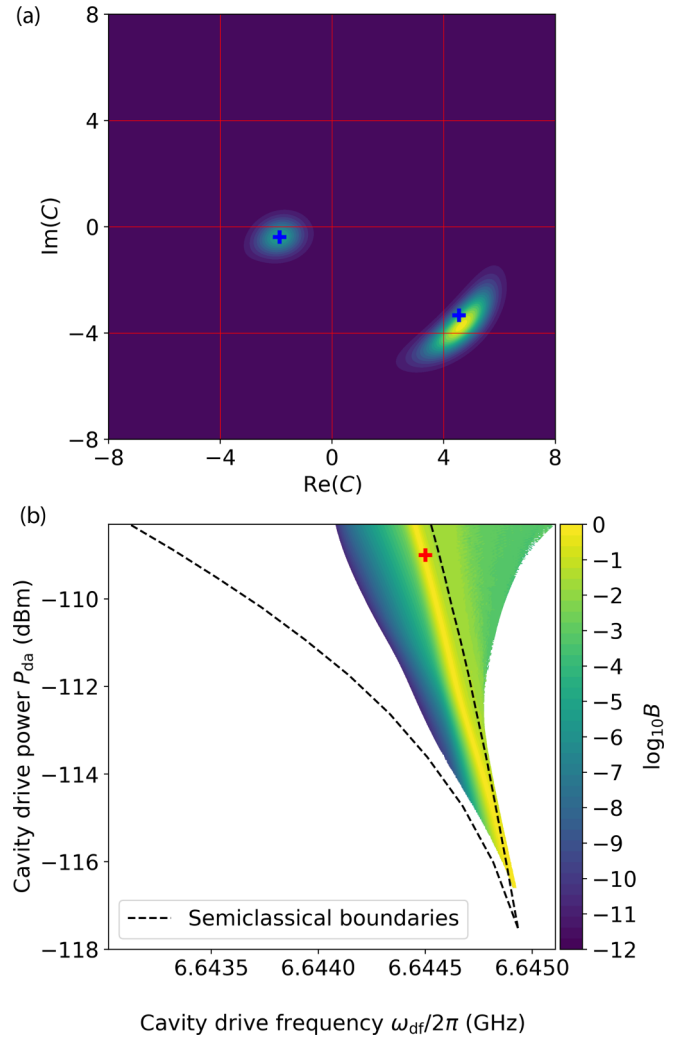


FIG. 5. The bistable regime. The cavity drive power is given by $P_{\text{da}} = 20 \log_{10}(\Omega_c/\omega_{2,0})$ where $\omega_{2,0}/2\pi = 340$ GHz. In (a) we plot the Wigner function of the cavity state in the bistable regime, which is obtained by solving for the steady state of the master equation at a drive power of $P_{\text{da}} = -109$ dBm and a drive frequency of $\omega_{\text{dr}}/2\pi = 6.6445$ GHz. These parameters are marked by the red crosses in (b) and in Fig. 4(b). Two metastable states can be seen: a bright state at $C_b = 4.64 - 3.73i$ and a dim state at $C_d = -1.88 - 0.39i$. These two states correspond to the fixed points produced using the semiclassical equations of motion, marked by blue crosses. Next in (b) we examine the boundaries of the bistable regime. By examining the cavity Wigner function over a range of drive powers and frequencies we map the region in which we find two peaks corresponding to the bright and dim states. When two peaks can be identified we calculate the metric $B = 1 - |p_b - p_d|$ as a measure of bistability. This is plotted in the color map above. Meanwhile the dashed black lines mark the boundaries of the region in which the semiclassical equations of motion have two fixed points. These methods produce significant overlap and both predict the onset of bistability around $P_{\text{da}} = -117$ dB. We also see that the region of maximum bistability predicted by the master equation (yellow strip) lies either close to or within the semiclassical bistable region at all powers. However, there are significant differences in the limits of the bistable region, particularly at the upper frequency limit. The master equation predicts this limit should increase with drive power, whereas the semiclassical equations predict the opposite.

ACKNOWLEDGMENTS

We are grateful to Sergey Shevchenko for very useful discussions and suggestions to improve the manuscript. The work of the Waterloo group is supported by NSERC and CMC and the work of the Technion group by the Israeli Science Foundation Grant No. 963/19.

E.B. and P.B. contributed equally to this work.

APPENDIX A: DRESSED STATES

In this Appendix the semiclassical dynamics of a driven qubit coupled to a cavity mode is discussed [48–54]. In the RWA the Hamiltonian \mathcal{H}_0 of the closed system in a frame rotated at the qubit driving angular frequency ω_p is given by (see Eq. (A13) of Ref. [46])

$$\begin{aligned} \hbar^{-1}\mathcal{H}_0 = & -\Delta_{\text{pa}}\Sigma_z + \frac{\Omega_q(\Sigma_+ + \Sigma_-)}{4} \\ & - \Delta_{\text{pc}}A^\dagger A + \frac{g_1(A\Sigma_- + \Sigma_+A^\dagger)}{2}, \end{aligned} \quad (\text{A1})$$

where $\Delta_{\text{pa}} = \omega_p - \omega_a$, $\hbar\omega_a$ is the qubit energy, Σ_z is the qubit longitudinal operator, Ω_q is the driving amplitude, Σ_+ and $\Sigma_- = \Sigma_+^\dagger$ are qubit rotated transverse operators, $\Delta_{\text{pc}} = \omega_p - \omega_c$, ω_c is the cavity mode angular frequency, $A^\dagger A$ is the cavity mode number operator, and g_1 is the coupling coefficient.

The Bloch equations of motion for the expectation values $a = \langle A \rangle$, $p_+ = \langle \Sigma_+ \rangle$, and $p_z = \langle \Sigma_z \rangle$ are obtained from the Heisenberg equations of motion and the commutation relations $[A, A^\dagger] = 1$, $[\Sigma_z, \Sigma_\pm] = \pm\Sigma_\pm$, and $[\Sigma_+, \Sigma_-] = 2\Sigma_z$ by adding fluctuation and dissipation terms and by averaging

$$\dot{a} = -(\gamma_c - i\Delta_{\text{pc}})a - \frac{ig_1 p_+}{2}, \quad (\text{A2})$$

$$\dot{p}_+ = -(\gamma_2 + i\Delta_{\text{pa}})p_+ - \frac{i\Omega_q p_z}{2} - ig_1 a p_z, \quad (\text{A3})$$

$$\dot{p}_z = -\gamma_1(p_z - p_0) + \frac{i\omega_1(p_+^* - p_+)}{4} + \frac{ig_1(ap_+^* - p_+a^*)}{2}, \quad (\text{A4})$$

where the overdot denotes time derivative, γ_c is the cavity mode damping rate, γ_1 and γ_2 are the qubit longitudinal and transverse damping rates, respectively, the coefficient $p_0 = -\tanh[(\hbar\omega_a)/(2k_B T)]$ is the value of p_z in thermal equilibrium (when $\Omega_q = g_1 = 0$), k_B is the Boltzmann's constant, and T is the temperature. In the absence of coupling, i.e., when $g_1 = 0$, the steady state solution of Eqs. (A3) and (A4) is given by $p_{+,ss} = -(i\Omega_q p_{z,ss})/(2\gamma_2 + 2i\Delta_{\text{pa}})$ and $p_{z,ss} = p_0[1 + (\gamma_2\Omega_q^2)/(4\gamma_1\gamma_2^2 + 4\gamma_1\Delta_{\text{pa}}^2)]^{-1}$.

Consider the transformation

$$\begin{pmatrix} \Sigma'_+ \\ \Sigma'_- \\ \Sigma'_z \end{pmatrix} = M_a \begin{pmatrix} \Sigma_+ \\ \Sigma_- \\ \Sigma_z \end{pmatrix}, \quad (\text{A5})$$

where

$$M_a = \begin{pmatrix} \frac{\sin\alpha+1}{2} & \frac{\sin\alpha-1}{2} & -\cos\alpha \\ \frac{\sin\alpha-1}{2} & \frac{\sin\alpha+1}{2} & -\cos\alpha \\ \frac{\cos\alpha}{2} & \frac{\cos\alpha}{2} & \sin\alpha \end{pmatrix}, \quad (\text{A6})$$

and where $\tan\alpha = (-2\Delta_{\text{pa}}/\Omega_q)$. Note that the transformed operators Σ'_\pm and Σ'_z satisfy the commutation relations $[\Sigma'_z, \Sigma'_\pm] = \pm\Sigma'_\pm$ and $[\Sigma'_+, \Sigma'_-] = 2\Sigma'_z$ provided that the original operators Σ_\pm and Σ_z satisfy $[\Sigma_z, \Sigma_\pm] = \pm\Sigma_\pm$ and $[\Sigma_+, \Sigma_-] = 2\Sigma_z$.

Under this transformation the first two terms of the Hamiltonian \mathcal{H}_0 (A1) become $-\Delta_{\text{pa}}\Sigma_z + \Omega_q(\Sigma_+ + \Sigma_-)/4 = (\omega_R/2)\Sigma'_z$, where $\omega_R = \sqrt{\Omega_q^2 + 4\Delta_{\text{pa}}^2}$ is the Rabi frequency. In the RWA, in which counter-rotating terms are disregarded, the equations of motion (A2), (A3), and (A4) are transformed into

$$\dot{a} = -(\gamma_c - i\Delta_{\text{pc}})a - \frac{ig'_1 p'_+}{2}, \quad (\text{A7})$$

$$\dot{p}'_+ = -\left(\gamma'_2 - \frac{i\omega_R}{2}\right)p'_+ - ig'_1 a p'_z, \quad (\text{A8})$$

$$\dot{p}'_z = -\gamma'_1(p'_z - p'_0) + \frac{ig'_1(ap'^*_+ - p'_+a^*)}{2}, \quad (\text{A9})$$

where the effective coupling coefficient g'_1 is given by $g'_1 = (1/2)(\sin\alpha + 1)g_1$, the transformed damping rates γ'_1 and γ'_2 are given by $\gamma'_1 = \gamma_2 + (\gamma_1 - \gamma_2)\sin^2\alpha$ and $\gamma'_2 = (1/2)(\gamma_1 + \gamma_2) + (1/2)(\gamma_2 - \gamma_1)\sin^2\alpha$, respectively, and the polarization coefficient p'_0 is related to p_0 by

$$p'_0 = \frac{\sin\alpha}{\frac{\gamma_2}{\gamma_1}(1 + \frac{\gamma_1 - \gamma_2}{\gamma_2}\sin^2\alpha)} p_0. \quad (\text{A10})$$

Note that the equations of motion (A7)–(A9) become unstable when [65–69]

$$g_1^2 \geq -\frac{2\gamma_c\gamma'_2}{p'_0} \left(1 + \frac{\Delta_L^2}{(\gamma_c + \gamma'_2)^2}\right), \quad (\text{A11})$$

where $\Delta_L = \Delta_{\text{pc}} - \omega_R/2$.

In the limit where the coupling coefficient g'_1 is sufficiently small, at and near steady state the term p'_z in Eq. (A8) can be approximately treated as a constant, and consequently Eqs. (A7) and (A8) can be expressed in a matrix form as

$$\frac{d}{dt} \begin{pmatrix} a \\ p'_+ \end{pmatrix} + M_P \begin{pmatrix} a \\ p'_+ \end{pmatrix} = 0, \quad (\text{A12})$$

where the matrix M_P is given by

$$M_P = \begin{pmatrix} \gamma_c - i\Delta_{\text{pc}} & \frac{ig'_1}{2} \\ ig'_1 p'_z & \gamma'_2 - \frac{i\omega_R}{2} \end{pmatrix}. \quad (\text{A13})$$

To lowest nonvanishing order in g' the eigenvalues of the matrix M_P are given by

$$\Gamma_c = \gamma_c - i\Delta_{\text{pc}} + \frac{\frac{p'_z g'^2}{2}}{\gamma'_2 - \gamma_c + i\Delta_L} + O(g'^4), \quad (\text{A14})$$

$$\Gamma_2 = \gamma'_2 - \frac{i\omega_R}{2} - \frac{\frac{p'_z g'^2}{2}}{\gamma'_2 - \gamma_c + i\Delta_L} + O(g'^4). \quad (\text{A15})$$

The real parts of Γ_c (Γ_2) represents the effective damping rates $\gamma_{c,\text{eff}}$ ($\gamma'_{2,\text{eff}}$) of the cavitylike (qubitlike) mode. As can be seen from Eqs. (A14) and (A15), in this limit the coupling gives rise to repulsionlike behavior of the damping rates, i.e., $|\gamma_{c,\text{eff}} - \gamma'_{2,\text{eff}}| > |\gamma_c - \gamma'_2|$ (it is assumed that $p'_z < 0$). This behavior can be considered as a generalization of the Purcell effect [10] for the case of dressed states.

APPENDIX B: SIMULATING LINE NARROWING

Experimentally we have observed narrowing in the cavity spectrum which occurs when a drive is applied to the qubit. In an attempt to model this narrowing we perform simulations of the cavity response by unraveling the Lindblad master equation using a quantum jump (Monte Carlo) stochastic Schrödinger equation. In a frame rotating with the qubit drive at angular frequency ω_p we use the rotating wave approximation (RWA) to write down the Hamiltonian as

$$\hbar^{-1}\mathcal{H}(t) = \hbar^{-1}\mathcal{H}_0 + \Omega_c[A \exp(i\Delta_{dp}t) + A^\dagger \exp(-i\Delta_{dp}t)], \quad (\text{B1})$$

where the time independent part of the Hamiltonian \mathcal{H}_0 is given in Eq. (A1) and the time dependent cavity drive oscillates at the frequency $\Delta_{dp} = \omega_{df} - \omega_p$. In order to describe dissipation due to loss of photons from the cavity we use the Lindblad operator $\sqrt{\gamma_c}A$, while to describe dissipation in the qubit we use $\sqrt{\gamma}\Sigma^-$. After combining these elements the evolution of the state of the system is described by

$$\partial_t \rho = -\frac{i}{\hbar}[\mathcal{H}(t), \rho] + \gamma_c \mathcal{D}[A]\rho + \gamma_1 \mathcal{D}[\Sigma^+]\rho. \quad (\text{B2})$$

We use this equation to numerically evolve the state $\rho(t)$ over time and study the cavity amplitude $\langle A \rangle = \text{Tr}[\rho(t)A]$. We find that the time dependence of $\langle A \rangle$ contains two main frequencies: Δ_{dp} and Δ_{cp} , due to the drive and cavity frequency, respectively. The experimental data presented in Fig. 3 were measured by mixing the signal transmitted through the cavity with a reference at the cavity drive frequency. Therefore, in order to model the transmitted power T_{NA} we must examine the cavity amplitude $\langle A \rangle$ in a frame rotating with the drive. This is given by

$$\alpha(\Delta_{dp}, t) = \text{Tr}[\rho(t)A] \exp(-i\Delta_{dp}t). \quad (\text{B3})$$

Input-output relations can then be used to calculate T_{NA} from this amplitude.

We now attempt to reproduce the spectrum seen in Fig. 3(b). In order to observe narrowing we must drive the cavity in the nonlinear regime. We take a cavity drive amplitude of $\Omega_c/2\pi = 1.00$ MHz. The remaining parameters are set to $\Omega_q/2\pi = 1.726$ MHz, $\omega_p/2\pi = 5.50$ GHz, $g_1/2\pi = 0.150$ GHz, $\omega_a/2\pi = 5$ GHz, $\omega_c/2\pi = 6.6408$ GHz, $\gamma_c/2\pi = 377$ kHz, and $\gamma_1/2\pi = 40.7$ kHz. Using these parameters we produce the spectrum in Fig. 6 by evolving the state of our system over 9.6 ms for a range of cavity drive frequencies. The long time average $\bar{\alpha}(\Delta_{dp})$ displays a full width at half maximum of 125 kHz, significantly less than the natural linewidth of 377 kHz.

This narrowing can be explained when we realize that in the presence of a strong cavity drive the system displays multistability and the line narrowing is due to a bright cavity state (b) which is most stable over a narrow range of frequencies close to the bare cavity resonance. Close to the cavity resonance the system occupies the bright state and the transmitted power is high. However, away from this point the system may also occupy two other dim states (d_\downarrow and d_\uparrow), which causes a sharp drop in the transmitted power and a narrow linewidth.

In Fig. 7 we examine these metastable states more closely. We plot the cavity amplitude and qubit polarization over

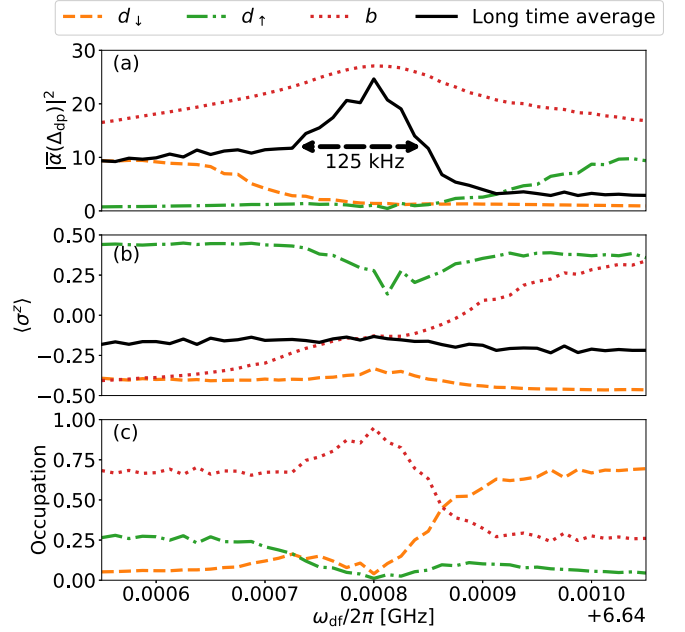


FIG. 6. Simulation of the cavity spectrum in the nonlinear regime. We use a cavity drive amplitude of $\Omega_c/2\pi = 1$ MHz, a qubit drive frequency of $\omega_p = 5.5$ GHz, and a qubit drive amplitude of $\Omega_q = 0.863$ GHz. The system displays multistability and three distinct metastable states can be identified, which are labeled by d_\downarrow , d_\uparrow , and b and assigned the colors orange, green, and red, respectively. We plot the square cavity amplitude (a), qubit polarization (b), and occupation probability (c) of each of these three states against the cavity drive frequency $\omega_{df}/2\pi$. In (a) we see that the cavity amplitude of state b is significantly larger than the amplitudes of states d_\downarrow and d_\uparrow . Hence we refer to b as bright and d_\downarrow and d_\uparrow as dim. The black line is produced by averaging the cavity amplitude over 9.6 ms of evolution before taking the square of the absolute value. It displays a narrow resonance at the bare cavity frequency. The full width at half maximum is only 125 kHz, which is 33% of the natural linewidth of 377 kHz. In (b) we see that states d_\downarrow and d_\uparrow occur when the qubit is polarized up and down, respectively, whereas the qubit polarization associated with state b varies with the drive frequency. Finally in (c) we see the occupation probabilities of the three states. Away from the cavity resonance the stability of state b falls. This causes the narrowing observed in (a).

170 μs of evolution at $\omega_d/2\pi = 6.6409$ GHz. The two dim states, labeled d_\uparrow and d_\downarrow , occur when the qubit is polarized in the up and down directions, respectively. Meanwhile the bright state occurs when the qubit is depolarized and varies widely over the range $-1 < \langle \sigma^z \rangle < 1$.

APPENDIX C: SPECTRA CALCULATIONS

In order to calculate the response of our system to cavity driving (without qubit driving) we use the following master equation:

$$\partial_t \rho = -i[\mathcal{H}/\hbar, \rho] + \gamma_c \mathcal{D}[A]\rho + \gamma_1 \mathcal{D}[\Sigma_+]\rho, \quad (\text{C1})$$

which consists of nonunitary components calculated according to $\mathcal{D}(L)\rho = L^\dagger \rho L - \frac{1}{2}(L^\dagger L \rho + \rho L^\dagger L)$ and a unitary

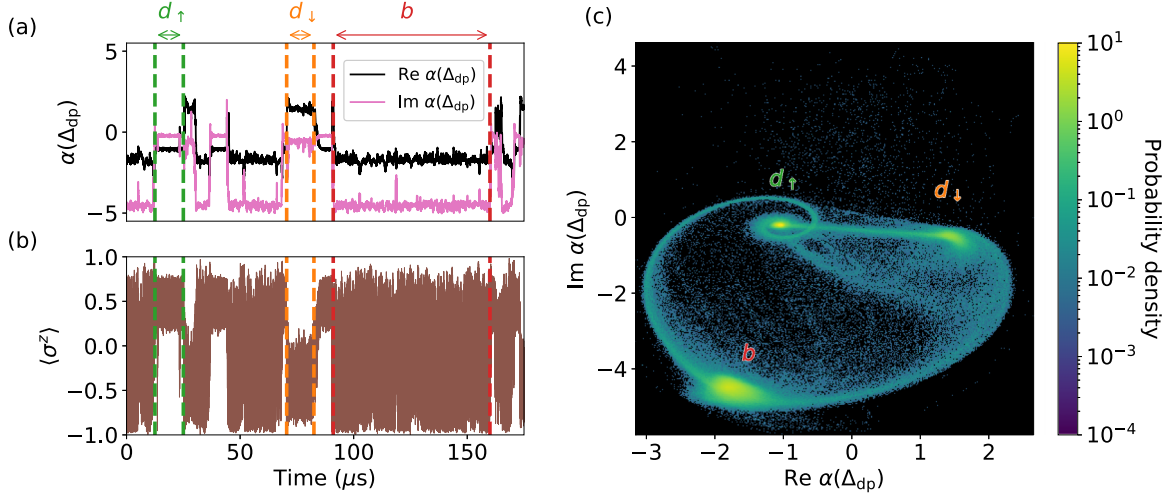


FIG. 7. Here we examine a quantum state trajectory produced at $\omega_{df}/2\pi = 6.6409$ GHz. In (a) we plot the real and imaginary parts of the cavity amplitude while in (b) we plot the polarization of the qubit. The cavity is observed to jump between three metastable states, examples of which are highlighted between the vertical dashed lines. At the top of (a) we label these states as d_{\uparrow} , d_{\downarrow} , and b . We note that states d_{\uparrow} and d_{\downarrow} have a significantly smaller cavity amplitude than state b , hence we say the first two states are dim and the third is bright. By referring to (b) we see that state d_{\uparrow} occurs when the qubit has positive polarization, state d_{\downarrow} occurs when it has negative polarization, and state b occurs when the qubit freely varies over the range $-1 < \langle \sigma^z \rangle < 1$. In (c) we plot a histogram of the cavity amplitude throughout 9.6 ms of evolution. The three metastable states are clearly identified as three clusters in the plane. Switching pathways leading between these clusters can also be observed.

component which obeys the Hamiltonian given by

$$\begin{aligned} \hbar^{-1}\mathcal{H} = & -\Delta_{da}\Sigma_z + \Omega_c(A^\dagger + A) \\ & -\Delta_{dc}A^\dagger A + \frac{g_1}{2}(\Sigma_- A + \Sigma_+ A^\dagger). \end{aligned} \quad (\text{C2})$$

In the above the detuning between the cavity drive and the cavity resonance is given by $\Delta_{dc} = \omega_{df} - \omega_c$, while the detuning between the cavity drive and the qubit frequency is given by $\Delta_{da} = \omega_{df} - \omega_a$. Since the relaxation rate of the qubit depends on the magnetic field detuning from the symmetry point we must take account of this in our calculations. For Figs. 4(a)–4(c) we have $\omega_f/2\pi = 5.5$ GHz and $\gamma_1/2\pi = 6.29$ kHz,

whereas for Figs. 4(d)–4(f) we have $\omega_f/2\pi = 7.8$ GHz and $\gamma_1/2\pi = 4.02$ kHz.

The master equation above does not include a Lindblad operator to describe pure dephasing of the flux qubit. Since we are operating the qubit far from its symmetry point, pure dephasing will be dominated by flux noise, and in [6] the power spectral density (PSD) of this noise was found to have a $1/f^{0.9}$ form. Unfortunately we cannot account for this noise in the master equation, because the Markovian approximation requires that the PSD is well behaved at zero frequency. However, even without the inclusion of pure dephasing, the master equation is still able to explain the major features of the spectra measured in Fig. 4.

-
- [1] G. Breit and E. Wigner, Capture of slow neutrons, *Phys. Rev.* **49**, 519 (1936).
 - [2] U. Fano, Effects of configuration interaction on intensities and phase shifts, *Phys. Rev.* **124**, 1866 (1961).
 - [3] A. Z. Devdariani, V. N. Ostrovskii, and Y. N. Sebyakin, Crossing of quasistationary levels, *Sov. Phys. JETP* **44**, 477 (1976).
 - [4] F.-M. Dittes, The decay of quantum systems with a small number of open channels, *Phys. Rep.* **339**, 215 (2000).
 - [5] H. Friedrich and D. Wintgen, Interfering resonances and bound states in the continuum, *Phys. Rev. A* **32**, 3231 (1985).
 - [6] J.-L. Orgiazzi, C. Deng, D. Layden, R. Marchildon, F. Kitapli, F. Shen, M. Bal, F. R. Ong, and A. Lupascu, Flux qubits in a planar circuit quantum electrodynamics architecture: Quantum control and decoherence, *Phys. Rev. B* **93**, 104518 (2016).
 - [7] V. B. Braginsky, M. L. Gorodetsky, F. Y. Khalili, and K. S. Thorne, Dual-resonator speed meter for a free test mass, *Phys. Rev. D* **61**, 044002 (2000).
 - [8] Q. Xu, S. Sandhu, M. L. Povinelli, J. Shakya, S. Fan, and M. Lipson, Experimental Realization of an On-Chip All-Optical Analog to Electromagnetically Induced Transparency, *Phys. Rev. Lett.* **96**, 123901 (2006).
 - [9] Y.-C. Liu, B.-B. Li, and Y.-F. Xiao, Electromagnetically induced transparency in optical microcavities, *Nanophotonics* **6**, 789 (2017).
 - [10] E. M. Purcell, Spontaneous emission probabilities at radio frequencies, in *Confined Electrons and Photons* (Springer, Berlin, 1995), pp. 839–839.
 - [11] G. E. Makhmetov, A. G. Borisov, D. Teillet-Billy, and J. P. Gauyacq, Interaction between overlapping quasi-stationary states: He (2^1S and 2^1P) levels in front of an aluminium surface, *Europhys. Lett.* **27**, 247 (1994).
 - [12] I. Seipp, K. T. Taylor, and W. Schweizer, Atomic resonances in parallel electric and magnetic fields, *J. Phys. B: At. Mol. Opt. Phys.* **29**, 1 (1996).

- [13] J. P. Marangos, Electromagnetically induced transparency, *J. Mod. Opt.* **45**, 471 (1998).
- [14] Y. Wu and X. Yang, Electromagnetically induced transparency in v -, λ -, and cascade-type schemes beyond steady-state analysis, *Phys. Rev. A* **71**, 053806 (2005).
- [15] D. Budker, D. F. Kimball, S. M. Rochester, and V. V. Yashchuk, Nonlinear Magneto-Optics and Reduced Group Velocity of Light in Atomic Vapor with Slow Ground State Relaxation, *Phys. Rev. Lett.* **83**, 1767 (1999).
- [16] M. Fleischhauer and M. D. Lukin, Quantum memory for photons: Dark-state polaritons, *Phys. Rev. A* **65**, 022314 (2002).
- [17] J. E. Mooij, T. P. Orlando, L. Levitov, L. Tian, C. H. Van der Wal, and S. Lloyd, Josephson persistent-current qubit, *Science* **285**, 1036 (1999).
- [18] T. P. Orlando, J. E. Mooij, L. Tian, C. H. van der Wal, L. S. Levitov, S. Lloyd, and J. J. Mazo, Superconducting persistent-current qubit, *Phys. Rev. B* **60**, 15398 (1999).
- [19] A. Wallraff, D. I. Schuster, A. Blais, L. Frunzio, R.-S. Huang, J. Majer, S. Kumar, S. M. Girvin, and R. J. Schoelkopf, Strong coupling of a single photon to a superconducting qubit using circuit quantum electrodynamics, *Nature (London)* **431**, 162 (2004).
- [20] T. Niemczyk, F. Deppe, H. Huebl, E. P. Menzel, F. Hocke, M. J. Schwarz, J. J. Garcia-Ripoll, D. Zueco, T. Hümmer, E. Solano *et al.*, Circuit quantum electrodynamics in the ultrastrong-coupling regime, *Nat. Phys.* **6**, 772 (2010).
- [21] P. Forn-Díaz, J. Lisenfeld, D. Marcos, J. J. García-Ripoll, E. Solano, C. J. P. M. Harmans, and J. E. Mooij, Observation of the Bloch-Siegert Shift in a Qubit-Oscillator System in the Ultrastrong Coupling Regime, *Phys. Rev. Lett.* **105**, 237001 (2010).
- [22] P. Forn-Díaz, L. Lamata, E. Rico, J. Kono, and E. Solano, Ultrastrong coupling regimes of light-matter interaction, *Rev. Mod. Phys.* **91**, 025005 (2019).
- [23] A. A. Abdumalikov, Jr., O. Astafiev, Y. Nakamura, Y. A. Pashkin, and J. S. Tsai, Vacuum Rabi splitting due to strong coupling of a flux qubit and a coplanar-waveguide resonator, *Phys. Rev. B* **78**, 180502(R) (2008).
- [24] M. Bal, C. Deng, J.-L. Orgiazzi, F. R. Ong, and A. Lupascu, Ultrasensitive magnetic field detection using a single artificial atom, *Nat. Commun.* **3**, 1324 (2012).
- [25] M. Jerger, S. Poletto, P. Macha, U. Hübner, E. Il'ichev, and A. V. Ustinov, Frequency division multiplexing readout and simultaneous manipulation of an array of flux qubits, *Appl. Phys. Lett.* **101**, 042604 (2012).
- [26] G. Oelsner, S. H. W. van der Ploeg, P. Macha, U. Hübner, D. Born, S. Anders, E. Il'ichev, H.-G. Meyer, M. Grajcar, S. Wünsch, M. Siegel, A. N. Omelyanchouk, and O. Astafiev, Weak continuous monitoring of a flux qubit using coplanar waveguide resonator, *Phys. Rev. B* **81**, 172505 (2010).
- [27] K. Inomata, T. Yamamoto, P.-M. Billangeon, Y. Nakamura, and J. S. Tsai, Large dispersive shift of cavity resonance induced by a superconducting flux qubit in the straddling regime, *Phys. Rev. B* **86**, 140508(R) (2012).
- [28] I. Serban, M. I. Dykman, and F. K. Wilhelm, Relaxation of a qubit measured by a driven duffing oscillator, *Phys. Rev. A* **81**, 022305 (2010).
- [29] C. Laflamme and A. A. Clerk, Quantum-limited amplification with a nonlinear cavity detector, *Phys. Rev. A* **83**, 033803 (2011).
- [30] I. Siddiqi, R. Vijay, F. Pierre, C. M. Wilson, M. Metcalfe, C. Rigetti, L. Frunzio, and M. H. Devoret, RF-Driven Josephson Bifurcation Amplifier for Quantum Measurement, *Phys. Rev. Lett.* **93**, 207002 (2004).
- [31] A. Lupascu, E. F. C. Driessen, L. Roschier, C. J. P. M. Harmans, and J. E. Mooij, High-Contrast Dispersive Readout of a Superconducting Flux Qubit using a Nonlinear Resonator, *Phys. Rev. Lett.* **96**, 127003 (2006).
- [32] E. Boaknin, V. E. Manucharyan, S. Fissette, M. Metcalfe, L. Frunzio, R. Vijay, I. Siddiqi, A. Wallraff, R. J. Schoelkopf, and M. Devoret, Dispersive microwave bifurcation of a superconducting resonator cavity incorporating a Josephson junction, [arXiv:cond-mat/0702445](https://arxiv.org/abs/cond-mat/0702445).
- [33] F. Mallet, F. R. Ong, A. Palacios-Laloy, F. Nguyen, P. Bertet, D. Vion, and D. Esteve, Single-shot qubit readout in circuit quantum electrodynamics, *Nat. Phys.* **5**, 791 (2009).
- [34] M. Boissonneault, J. M. Gambetta, and A. Blais, Nonlinear dispersive regime of cavity QED: The dressed dephasing model, *Phys. Rev. A* **77**, 060305(R) (2008).
- [35] M. Boissonneault, J. M. Gambetta, and A. Blais, Improved Superconducting Qubit Readout by Qubit-Induced Nonlinearities, *Phys. Rev. Lett.* **105**, 100504 (2010).
- [36] M. Boissonneault, A. C. Doherty, F. R. Ong, P. Bertet, D. Vion, D. Esteve, and A. Blais, Superconducting qubit as a probe of squeezing in a nonlinear resonator, *Phys. Rev. A* **89**, 022324 (2014).
- [37] M. Boissonneault, A. C. Doherty, F. R. Ong, P. Bertet, D. Vion, D. Esteve, and A. Blais, Back-action of a driven nonlinear resonator on a superconducting qubit, *Phys. Rev. A* **85**, 022305 (2012).
- [38] M. Boissonneault, J. M. Gambetta, and A. Blais, Dispersive regime of circuit QED: Photon-dependent qubit dephasing and relaxation rates, *Phys. Rev. A* **79**, 013819 (2009).
- [39] M. D. Reed, L. DiCarlo, B. R. Johnson, L. Sun, D. I. Schuster, L. Frunzio, and R. J. Schoelkopf, High-Fidelity Readout in Circuit Quantum Electrodynamics using the Jaynes-Cummings Nonlinearity, *Phys. Rev. Lett.* **105**, 173601 (2010).
- [40] F. R. Ong, M. Boissonneault, F. Mallet, A. C. Doherty, A. Blais, D. Vion, D. Esteve, and P. Bertet, Quantum Heating of a Nonlinear Resonator Probed by a Superconducting Qubit, *Phys. Rev. Lett.* **110**, 047001 (2013).
- [41] F. R. Ong, M. Boissonneault, F. Mallet, A. Palacios-Laloy, A. Dewes, A. C. Doherty, A. Blais, P. Bertet, D. Vion, and D. Esteve, Circuit QED with a Nonlinear Resonator: Ac-Stark Shift and Dephasing, *Phys. Rev. Lett.* **106**, 167002 (2011).
- [42] L. S. Bishop, J. M. Chow, J. Koch, A. A. Houck, M. H. Devoret, E. Thuneberg, S. M. Girvin, and R. J. Schoelkopf, Nonlinear response of the vacuum Rabi resonance, *Nat. Phys.* **5**, 105 (2009).
- [43] V. Peano and M. Thorwart, Quasienergy description of the driven Jaynes-Cummings model, *Phys. Rev. B* **82**, 155129 (2010).
- [44] J. Hausinger and M. Grifoni, Qubit-oscillator system under ultrastrong coupling and extreme driving, *Phys. Rev. A* **83**, 030301(R) (2011).
- [45] L. S. Bishop, E. Ginossar, and S. M. Girvin, Response of the Strongly Driven Jaynes-Cummings Oscillator, *Phys. Rev. Lett.* **105**, 100505 (2010).

- [46] E. Buks, C. Deng, Jean-Luc F. X. Orgazzi, M. Otto, and A. Lupascu, Superharmonic resonances in a strongly coupled cavity-atom system, *Phys. Rev. A* **94**, 033807 (2016).
- [47] Y.-F. Xie, L. Duan, and Q.-H. Chen, Generalized quantum Rabi model with both one- and two-photon terms: A concise analytical study, *Phys. Rev. A* **99**, 013809 (2019).
- [48] B. R. Mollow, Stimulated emission and absorption near resonance for driven systems, *Phys. Rev. A* **5**, 2217 (1972).
- [49] G. S. Agarwal, W. Lange, and H. Walther, Intense-field renormalization of cavity-induced spontaneous emission, *Phys. Rev. A* **48**, 4555 (1993).
- [50] M. Lewenstein and T. W. Mossberg, Spectral and statistical properties of strongly driven atoms coupled to frequency-dependent photon reservoirs, *Phys. Rev. A* **37**, 2048 (1988).
- [51] A. Kowalewska-Kudlaszyk and R. Tanaś, Generalized master equation for a two-level atom in a strong field and tailored reservoirs, *J. Mod. Opt.* **48**, 347 (2001).
- [52] J. Zakrzewski, M. Lewenstein, and T. W. Mossberg, Theory of dressed-state lasers. I. Effective Hamiltonians and stability properties, *Phys. Rev. A* **44**, 7717 (1991).
- [53] P. Zhou and S. Swain, Dynamics of a driven two-level atom coupled to a frequency-tunable cavity, *Phys. Rev. A* **58**, 1515 (1998).
- [54] C. Cohen-Tannoudji, J. Dupont-Roc, and G. Grynberg, Atom-photon interactions: Basic processes and applications, in *Atom-Photon Interactions: Basic Processes and Applications* (Wiley, Berlin, 1998), p. 678.
- [55] J. Gambetta, A. Blais, M. Boissonneault, A. A. Houck, D. I. Schuster, and S. M. Girvin, Quantum trajectory approach to circuit QED: Quantum jumps and the Zeno effect, *Phys. Rev. A* **77**, 012112 (2008).
- [56] S. Mukamel, I. Oppenheim, and J. Ross, Statistical reduction for strongly driven simple quantum systems, *Phys. Rev. A* **17**, 1988 (1978).
- [57] J. Li, M. P. Silveri, K. S. Kumar, J.-M. Pirkkalainen, A. Vepsäläinen, W. C. Chien, J. Tuorila, M. A. Sillanpää, P. J. Hakonen, E. V. Thuneberg *et al.*, Motional averaging in a superconducting qubit, *Nat. Commun.* **4**, 1420 (2013).
- [58] D. S. Karpov, V. Y. Monarkha, D. Szombati, A. G. Frieiro, A. N. Omelyanchouk, E. Il'ichev, A. Fedorov, and S. N. Shevchenko, Probabilistic motional averaging, *Eur. Phys. J. B* **93**, 49 (2020).
- [59] O. V. Ivakhnenko, S. N. Shevchenko, and F. Nori, Simulating quantum dynamical phenomena using classical oscillators: Landau-Zener-Stückelberg-Majorana interferometry, latching modulation, and motional averaging, *Sci. Rep.* **8**, 12218 (2018).
- [60] D. Szombati, A. Gomez Frieiro, C. Müller, T. Jones, M. Jerger, and A. Fedorov, Quantum Rifling: Protecting a Qubit from Measurement Back Action, *Phys. Rev. Lett.* **124**, 070401 (2020).
- [61] C. P. Slichter, *Principles of Magnetic Resonance* (Springer Science & Business Media, New York, 2013), Vol. 1.
- [62] T. K. Mavrogordatos, G. Tancredi, M. Elliott, M. J. Peterer, A. Patterson, J. Rahamim, P. J. Leek, E. Ginossar, and M. H. Szymańska, Simultaneous Bistability of a Qubit and Resonator in Circuit Quantum Electrodynamics, *Phys. Rev. Lett.* **118**, 040402 (2017).
- [63] T. K. Mavrogordatos, F. Barratt, U. Asari, P. Szafulski, E. Ginossar, and M. H. Szymańska, Rare quantum metastable states in the strongly dispersive Jaynes-Cummings oscillator, *Phys. Rev. A* **97**, 033828 (2018).
- [64] P. D. Drummond and D. F. Walls, Quantum theory of optical bistability. I. Nonlinear polarisability model, *J. Phys. A: Math. Gen.* **13**, 725 (1980).
- [65] O. Kocharovskaya, Amplification and lasing without inversion, *Phys. Rep.* **219**, 175 (1992).
- [66] J. Hauss, A. Fedorov, C. Hutter, A. Shnirman, and G. Schön, Single-Qubit Lasing and Cooling at the Rabi Frequency, *Phys. Rev. Lett.* **100**, 037003 (2008).
- [67] J. Hauss, A. Fedorov, S. André, V. Brosco, C. Hutter, R. Kothari, S. Yeshwanth, A. Shnirman, and G. Schön, Dissipation in circuit quantum electrodynamics: Lasing and cooling of a low-frequency oscillator, *New J. Phys.* **10**, 095018 (2008).
- [68] S. André, V. Brosco, M. Marthaler, A. Shnirman, and G. Schön, Few-qubit lasing in circuit QED, *Phys. Scr.* **2009**, 014016 (2009).
- [69] O. Astafiev, A. M. Zagoskin, A. A. Abdumalikov, Y. A. Pashkin, T. Yamamoto, K. Inomata, Y. Nakamura, and J. S. Tsai, Resonance fluorescence of a single artificial atom, *Science* **327**, 840 (2010).